Time-thermo-dynamics of anti-Stokes and Stokes scattering and luminescence in 1-nm silicon nanoparticles

Nayfeh, Munir H.; Morgan, Huw; Nayfeh, Ammar; Bahceci, Ersin; Abuhassan, Laila

Published in:
AIP Advances

DOI:
10.1063/5.0091537

Publication date:
2022

Citation for published version (APA):
Nayfeh, M. H., Morgan, H., Nayfeh, A., Bahceci, E., & Abuhassan, L. (2022). Time-thermo-dynamics of anti-Stokes and Stokes scattering and luminescence in 1-nm silicon nanoparticles: Toward an optical nanorefrigerator. *AIP Advances*, *12*(6), [5219]. https://doi.org/10.1063/5.0091537

AIP Advances

Time–thermo-dynamics of anti-Stokes and Stokes scattering and luminescence in 1-nm silicon nanoparticles: Toward an optical nanorefrigerator

Cite as: AIP Advances **12**, 065219 (2022); https://doi.org/10.1063/5.0091537
Submitted: 15 March 2022 • Accepted: 13 May 2022 • Published Online: 21 June 2022

Munir H. Nayfeh, Huw Morgan, Ammar Nayfeh, et al.

Time–thermo-dynamics of anti-Stokes and Stokes scattering and luminescence in 1-nm silicon nanoparticles: Toward an optical nanorefrigerator

Cite as: AIP Advances 12, 065219 (2022); doi: 10.1063/5.0091537
Submitted: 15 March 2022 • Accepted: 13 May 2022 •
Published Online: 21 June 2022

Munir H. Nayfeh,[1] Huw Morgan,[2] Ammar Nayfeh,[3,a)] Ersin Bahceci,[4] and Laila Abuhassan[5]

AFFILIATIONS

[1] Department of Physics, University of Illinois at Urbana-Champaign, 1110 W. Green Street, Urbana, Illinois 61801, USA
[2] Department of Physics, Aberystwyth University, Penglais, Aberystwyth, Ceredigion SY23 3BZ, United Kingdom
[3] Electrical Engineering and Computer Science, Khalifa University, Abu Dhabi 127788, United Arab Emirates
[4] Department of Metallurgical and Materials Engineering, Iskenderun Technical University, 31200 Hatay, Turkey
[5] Department of Physics, University of Jordan, Amman, Jordan

[a)] **Author to whom correspondence should be addressed:** m-nayfeh@illinois.edu

ABSTRACT

The thermodynamics of nanosystems is interesting, as they constitute the transition between the atomistic and solid states. This is empowered by the development of tools to manipulate individual atoms and perform atomistic simulations and fundamental thermos-science, such as microscopic time-symmetry and macroscopic time-asymmetry, the origin of time's arrow, and photo-cryo-refrigeration. We examine here the photo-thermo and time dynamics in 1-nm silicon nanoparticles with tetrahedral-molecular core–shell structure prepared *ex situ* and suspended in solvents or re-constituted in films. We examined the temperature dependence of the quantum efficiency and time-dynamics of the Stokes luminescence and its energy dependence across the band. With temperature, we get flat lifetimes but with delay in the onset in agreement with a model calculation of above barrier emission. Our atomistic time-dependent density functional theory shows that Stokes heating takes place in the molecular-like shell where the lifetime is in the nanosecond regime, whereas anti-Stokes cooling takes place in the tetrahedral core where the lifetime is in the ms regime. Unlike doped glasses, we observed a 2-order of magnitude increase in the quantum efficiency of the Stokes luminescence at 10° K. The increase in the quantum efficiency at low temperature, the high quantum efficiency of stimulated anti-Stokes scattering and its anti-correlation with the luminescence, and the visible transparency/blindness due to quantum confinement are requirements for solid state photo-cooling, which may afford an all-silicon photo-cryo-refrigeration, with potential full integration into the CMOS silicon industry.

I. INTRODUCTION

Entropy (disorder/randomness) and the laws of thermodynamics, especially the second law, have recently simulated a large volume of research[1–4] with discussions raging on its relation to the direction of time, both in the classical world, where the statistical thermodynamics regime holds with time being irreversible, and in the quantum world, where single events are important with time being reversible. One important aspect, which is presently under heavy investigation, is photo-matter interaction and the direction of heat transfer. In the case of atomic gas, this interaction leads to the cooling of the gas when the energy extracted by photon emission exceeds the energy introduced by photon absorption (exploiting relativity/Doppler effect). The energy difference is drawn from the translational kinetic energy of the atoms according to the relativity/Doppler effect law.[5] In contrast,[6] laser cooling of macroscopic

samples of condensed matter occurs when the additional energy of the emitted photons must be taken out of the collective atomic vibrations of the entire illuminated sample, i.e., the sample acts as a heat reservoir. As such, the process is in violation of Stokes' law and, hence, was coined anti-Stokes photoluminescence (ASPL).[7] Stokes law stipulates that the interaction results in heat (collective vibrations) taken from the electric/photon energy of the system. Moreover, the anti-Stokes process seemed to be in violation of the second law of thermodynamics since there is an entropy loss in the sample. However, the thermodynamic viability of the anti-Stokes process was resolved by Landau[8,9] by accounting for the contribution of the incident and emitted photons to the entropy of the system. He showed theoretically that the entropy lost by the sample upon cooling is compensated by an increase in the entropy of the light photons because of the loss of monochromaticity and beam directionality.[8,9]

Successful cooling of solids has been achieved in limited situations by implanting/doping ions in the solid such that the ions play the role of the fluorescing agent. An example of this is implanting rare-earth atoms in a host glass solid.[10–12] Using thulium-doped glass, cooling by more than 70° K has been attained.[13] However, due to their use in a variety of optoelectronic devices, and their promise of providing cooling to a temperature of 10° K as compared to 70° K, it is far more desirable to achieve laser cooling in homogeneous systems (semiconductors). However, it has been proven experimentally that such cooling by anti-Stokes photoluminescence ASPL in the condensed phase is more difficult to achieve. The difficulty may be understood when considering the requirements of the process. These include high photoluminescence quantum-efficiency (low non-radiative recombination rate), strong anti-Stokes transition (strong coupling between phonons and excited states), weak trapping, and reabsorption, i.e., optical transparency and escape of the anti-Stokes emission, which otherwise would cause re-heating of the sample. Despite numerous experimental attempts,[14–18] net laser-cooling in the semiconductor has only lately been reported due to the above challenges.

Cooling challenges in semiconductors can be significantly alleviated by employing quantum-confined nanostructures.[14] The novel optical and thermal characteristics of nanostructures and the development of ever more sophisticated experimental tools to manipulate individual molecules, and the widespread use of all-atom simulations empowered the growing interest in the thermodynamics of small systems.[19] For instance, the problem of light extraction is remedied when the emission wavelength is larger than the size of the nanostructure. In contrast to bulk semiconductors or heterostructures, the quantum efficiency of some nanostructures, such as double-heterostructure GaAs/GaInP nanostructures, can be enhanced to close to unity over a wide range of temperatures;[20,21] as well as improving the efficiency of ASPL processes.[22–31] In the nanosystem, the number of atoms is countable (finite), and as such, they may not be pure solids nor pure atoms/molecules, rather they constitute the transient between them. While the second law emerges from the statistics of huge numbers, nanosystems afford the study of relatively few degrees of freedom. For instance, the study of small systems affords the opportunity to examine the question of how can microscopic equations of motion that are symmetric with respect to time reversal give rise to macroscopic behavior that clearly does not share this symmetry (the origin of time's arrow). Nanosystems may also show some surprises when testing the second law of thermodynamics under non-equilibrium conditions.[32–34] Scientists found that in a silica nanoparticle trapped and cooled, heat flows from cold to hot.[32] After fast deposition of energy in the 1-nm nanoparticle using femtosecond light, the particle suffers structural relaxation into an equilibrium geometry with reduced bandgap, releasing light with less heat and entropy of the system.[33] A 50-nm-thick membrane of silicon nitride creates more entropy when measuring time more accurately.[34]

Among all semiconductors, silicon is the most challenging since it is an indirect bandgap material. Yet, silicon is highly rewarding at the nanoscale.[33,35–38] For instance, sub-3-nm, in general, and 1-nm Si nanoparticles, in particular, are unique by being not a pure solid bulk, but rather a mix of solid and molecule natures. Being at the transition of solid and molecule phases, much of the characteristics that are most applicable to bulk may not be fully applicable, affording novel characteristics. Novel characteristics include reduction of non-radiative dangling defects (Pb-centres), and capture rate on them,[35] strong optical nonlinearity,[36–39] high luminescence quantum efficiency, strong anti-Stokes light scattering,[40] stimulated and laser gain coefficients,[41,42] blindness (transparency) to visible radiation, resulting from quantum confinement,[43–45] as well as drop in the refractive index. Despite those interesting characteristics, there remain challenging fundamental issues relevant to thermodynamic applications. These include understanding the interconnection between the solid/molecule natures with regard to cooling and heating processes, Stokes and anti-Stokes processes, quantum efficiency, onset and lifetime, as well as the wavelength dependence of the luminesce band, as well as their thermal characteristics, especially at low temperature down to 10° K. This is pivotal in view of the fact that for a rare-earth-doped system, the population at the top of the ground state manifold of energy levels dramatically decreases as the temperature drops below 100° K, strongly reducing the efficiency of the cooling process. On the other hand, semiconductors are promising materials because, unlike implanted ions, the lower energy valence band is expected to be populated even at temperatures close to absolute zero because they are governed by Fermi–Dirac statistics.[46–50]

In this paper, we examine photo-luminescence and time dynamics of 1-nm silicon nanoparticles prepared *ex situ* and reconstituted in thin films on silicon wafers or dissolved in organic solvents. We conduct thermal studies of the intensity, quantum efficiency, and the lifetime dynamics of the luminescence over the range of 300°–10° K. We record the time dynamics of the Stokes luminescence (lifetime and onset of emission) and the temperature dependence over the range of 300°–100° K, as well as the wavelength dependence across the luminescence band. We also examine the temperature dependence of the quantum efficiency of luminescence for temperatures over the range of 300°–10° K. Our results show, unlike rare-earth-doped glass, a 1–2-order of magnitude increase of the quantum efficiency at low temperatures because of Fermi–Dirac statistics and time delay in the onset of the photoluminescence. We perform atomistic time-dependent density functional theory (TDDFT) calculation to determine the time dynamics of absorption and emission as well as develop a model for understanding the thermal Stokes emission above the barrier between the solid and molecular states. The measurements are consistent with time dynamics obtained from atomistic TDDFT calculation of the ground

state (HOMO) and the first excited state (LUMO) as well as emission time dynamics over the indirect, direct, and transition regimes. The features are also in agreement with a rate equation model developed for above-barrier thermal emission. The atomistic simulations indicate that the anti-Stokes cooling process occurs in the tetrahedral indirect regime in which the emission lifetime is in the millisecond regime, while the Stokes heating process occurs in the molecular regime where the emission lifetime is in the nanosecond regime. Photon cooling via anti-Stokes photoluminescence promises to realize all-solid-state photo-cryo-refrigeration. Small optical nanosilicon refrigerators afford the potential for full integration into the CMOS silicon industry, while *ex situ* synthesis with a high degree of reproducibility allows better control and manipulation of device fabrication. Moreover, nanosilicon affords the potential for full integration into the CMOS silicon industry, as well as a high degree of reproducibility and control in their fabrication and manipulation.

II. EXPERIMENTAL PROCEDURES

A. Synthesis of Si nanoparticles and their prototype configuration

The nanoparticles are produced by dispersing silicon wafers.[36–39,51–53] The wafers are ⟨100⟩ oriented, 1–10 Ω cm resistivity, *p*-type boron doped silicon. The process uses lateral anodization in a mixture of hydrogen peroxide and HF acid. The particles produced are H-passivated with a mono-hydride. Subsequent immersion in ultrasound acetone or water bath dislodges the ultrasmall particles from the top layer of the wafer. Excitation of the particle solution by radiation at 355 nm produces deep blue emission, which is observable with the naked eye, in room light. High-resolution transmission electron microscopy (TEM) of a thin graphite grid, which was coated with the particles, shows that the particles are 1 nm in diameter with 10% dispersion. A photon counting spectrofluorometer with a Xe arc-lamp light source excitation and 4 nm bandpass excitation and emission monochromators is used to record under ambient conditions the photoluminescence spectra of a colloid in isopropyl alcohol. The emission spectrum from a typical sample under 350 (365) nm UV excitation is shown in Fig. 1(a). A distinct emission band is observed centered at 440 nm and a weaker band at 480 nm. High-resolution TEM was used to image the particles as shown in Fig. 1(b).

Figure 1(c) shows a qualitative cartoon of the formation of the 1 nm particle configuration.[36–39] The structural prototype is arrived at by first carving out a sphere of 1-nm diameter from a single crystalline silicon wafer. The sphere contains 29 silicon atoms and 36 broken bonds. The 36 broken bonds are terminated with hydrogen atoms. The bandgap of the particle is fine-tuned by stripping pairs of nearby hydrogen atoms allowing the silicon atoms to reconstruct forming Si–Si bonds, resulting in a $Si_{29}H_{24}$ structure with a bandgap of 3.5 eV, close to the experimental value. The geometry optimizations were carried out using density functional generalized gradient approximations with a PW91 functional and 6-31G* and 6-31G** basis sets. The relaxed configuration (*T*d symmetry) shows five atoms constituting a single tetrahedral core and 24 atoms constituting a H-terminated reconstructed surface or shell ($Si_{29}H_{24}$), with six reconstructed dimers, and a center atom.[33] The $Si_{29}H_{24}$ particle is a mix of solid and molecule states, exhibiting solid-like behavior as well as molecule-like behavior.

B. Film sample preparation

For the lifetime measurements, a colloid or suspension is formed. Several samples are prepared in isopropyl, benzene, and THF. The quality of samples is checked by excitation with UV radiation to ensure the presence of the characteristic blue luminescence. The luminescence of colloid samples can be seen with the naked eye under irradiation by a laser beam at a wavelength in the range of 254–400 nm or by an incoherent Hg UV lamp at a wavelength of 365, 300, or 254 nm.

For nonlinear optical studies, Si particles are precipitated by dropping a large volume from a water colloid on a device quality silicon or glass wafer. The water is allowed to dry over an extended period (days) to allow the nanoparticles to self-assemble and reconstitute into a thin close-packed film (a few micrometers thick). Under drying and solidification, the thin film shatters into irregular micrometer sized amorphous pieces due to mechanical strain. Crystals of 50–100 μm across that are transparent (see-through) can be easily made. For the low temperature measurements, small volumes of the nanoparticle are drop-dried from an isopropyl colloid. Since alcohol dries quickly, particles dry before they had the chance to recrystallize, making thin films of random, very small amorphous crystals. When the precursor colloid is a soup of nanoparticles of several sizes, such as 1, 1.67, 2.2, and 3 nm, which luminesce in the blue, green, orange, and red parts of the optical spectrum, respectively, one can see, using UV irradiation, that the same size particles are assembled. Luminescent photos taken under UV irradiation of a film prepared on the device quality silicon using electro-deposition from an alcohol colloid show crystals with different colors of luminescence.

C. Measurement procedures

1. Time-resolved photoluminescence

The apparatus uses a single-photon pulsed laser excitation to excite a sample's fluorescence. The laser excitation source is a second harmonic of a solid state diode-pumped mode-locked Ti:sapphire laser with 150 fs pulses operating at an 80 MHz repetition rate.[38,54] The mode-locked output is frequency doubled by a potassium di-deuterium phosphate (KDP) nonlinear crystal. The fluorescence from the nanoparticle suspension is measured by a grating monochromator. The 80 MHz repetition rate of the excitation laser sets an observable time window of 12.5 ns. Two geometries were used in the acquisition of photoluminescence data. In the "vertical" configuration, the excitation beam is directed vertically through the base of a quartz nanoparticle colloid cuvette.

2. Quantum efficiency procedures

The quantum efficiency with temperature was measured using a single photon excitation scheme as follows. Thin films of nanoparticles were placed in the vacuum chamber and cooled to 10° K. The setup provides a resolution of 2 meV (0.05 Å). For detection over extended photon ranges, GaAs-based photocathode tubes are used (GaAs and GaInAs:Ce).

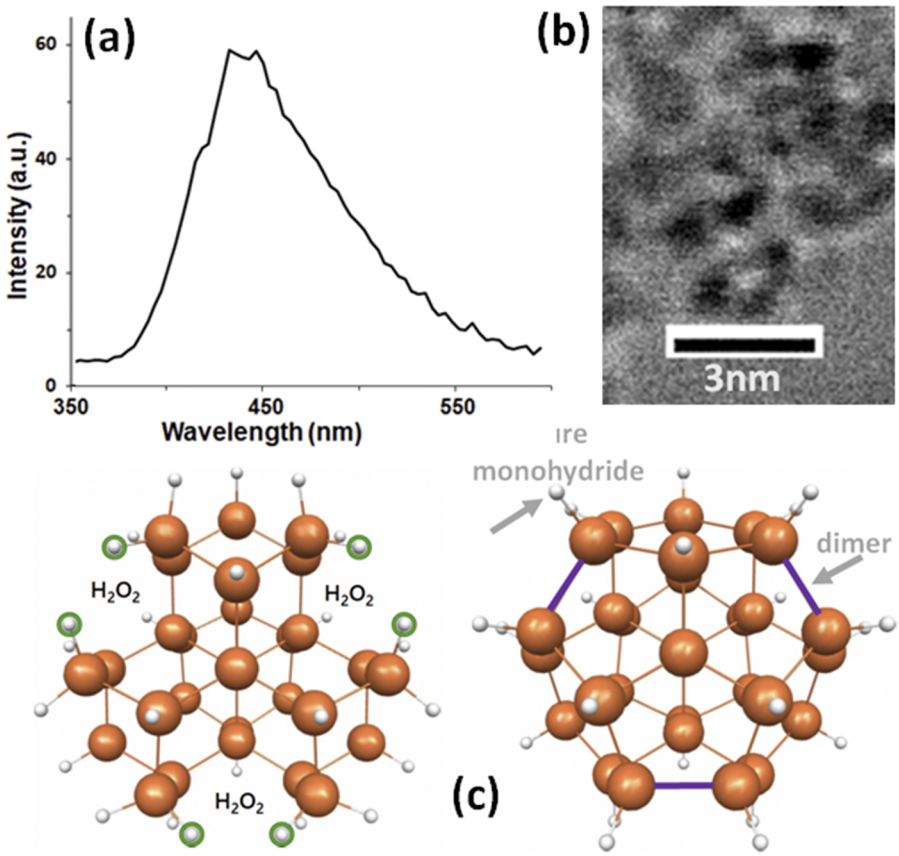

FIG. 1. (a) The emission spectrum from one of the samples under 350 nm UV excitation. A distinct emission band is observed, which is centered at 440 nm, and a weaker band at 480 nm. (b) High-resolution TEM image of the 1-nm silicon particles. (c) A qualitative cartoon description of the formation of the 1 nm particle configuration. A sphere of 1 nm diameter is carved out. A realistic structural prototype started from a single crystalline silicon wafer. The sphere contains 29 silicon atoms and has 36 broken bonds. The 36 broken bonds are terminated with hydrogen atoms and cleaned to a single Si–H of 24 hydrogen atoms. The number 29 is a magic number for the *T*d symmetry and spherical shape.

III. EXPERIMENTAL RESULTS

A. Thermal dependence of Stokes-luminescence lifetime

We measured the Stokes luminescence lifetime using a low density colloid of the nanoparticles as a function of temperature. We made measurements at different temperatures. Figures 2(a)–2(c) show the experimental time traces at the three temperatures 291°, 180°, and 130° K. They were taken under 780 nm excitation. The working range of the free decay is ~2–11 ns within the 0–12 ns duty cycle. Figure 2(a) shows that the background is ~10% of the maximum yield. This value of the background shows that the 1-nm nanoparticle has predominantly short lifetimes of ~12 ns. We analyze the time dynamics to a single exponential function and a constant that may account for any decay with a long time characteristic. The procedure yields 2.6 ± 0.3 ns for the lifetime. We next analyzed the decay to multiple decay rates. For two rates, we get lifetimes of 1 and 3 ns with amplitude branching ratios of 1–4 and a 5% constant.

We observe no change in the lifetime at different temperatures in this range. However, a sizable shift in the onset of decay is observed, especially at the lower temperature. The vertical line highlights the 0.28 ± 0.08 ns peak shift at low temperature. The emission is fast but the population transfer is sensitive to temperature. It

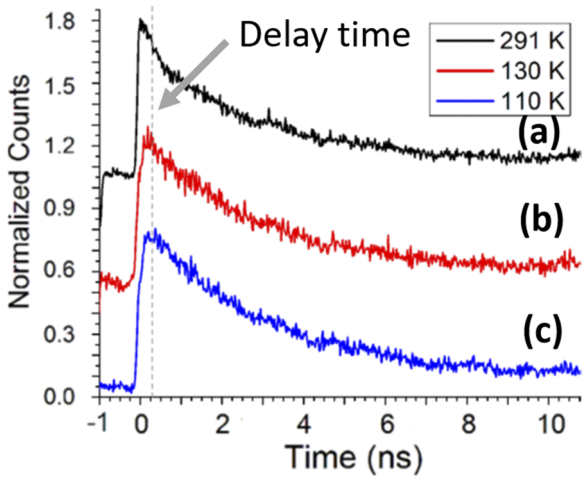

FIG. 2. Time-resolved photoluminescence in a typical trace *at room temperature*, taken under 780 nm excitation. The working range of the free decay is ~2–11 ns within the 0–12 ns duty cycle. The flat steady-state background is due to the accumulation from decay rates with a long characteristic time scale. (a)–(c) Experimental time traces at the three temperatures 291°, 180°, and 130° K, respectively. The vertical line in (a)–(c) is at 0.28 ± 0.08 ns peak shift at low temperature.

shows that the buildup of the population of the emitting state is faster at a higher temperature. This points to the presence of a potential barrier between the absorption and emission channels, which will be analyzed below.

We also measured the lifetime for different excitation wavelengths. Measurements using 800 nm excitation gave 1 and 3 ns with a 1–4 amplitude ratio and a 6% background constant. Measurements using 760 nm excitation gave 1 and 3 ns with a 1–4 amplitude ratio and a 7% constant. Setting the constant to near zero, the fit gives rates of 1.6 and 6 ns with an amplitude ratio of 1.3 to 1. The variation of rates with wavelength is found to be insignificant.

B. Wavelength dependence of lifetime of luminescence

We explored the energy dependence of the radiative lifetime by conducting experiments at different detection photon energies. We also used different solvents and orientations of the detection slit, as shown in Fig. 3. The error bars shown represent the standard deviation in the lifetime fitting parameters as reported by the fitting routine. In all room temperature measurements, the nanoparticle decays required two exponential terms to adequately describe the decay, one ~3 ns component and one ~0.5 ns component as shown. The long component had the largest amplitude at all emission energies except those with a strong solvent Raman signal.

C. Temperature dependence of the quantum efficiency

We examined the strength of the photoluminescence as a function of temperature in the range of 300°–10° K. We used the incident photon energy from a synchrotron source in the range of 4.8–22 eV. Figure 4(a) presents the luminescence spectrum with the sample cooled to 10° K and under excitation with an incident photon energy of 5.4 eV. The luminescence is measured over the range of 250–650 nm using a 250 nm blaze grating. The spectrum shows multiple wide luminescence bands in the UV at 265, 310, and 350 nm, as well as a visible band in the deep blue. The blue band, which peaks at 425 nm, commences at 380 nm and has a long wavelength tail as deep as 580 nm. The blue band is the lowest lying visible luminescence band. We should note that the observed bands are overlapping enough to constitute an underlying near continuum. Figure 4(b) shows the intensity at the peak of the blue band at 430 nm as a function of temperature. The intensity decays monotonically as the temperature increases, i.e., the response does not show intensity

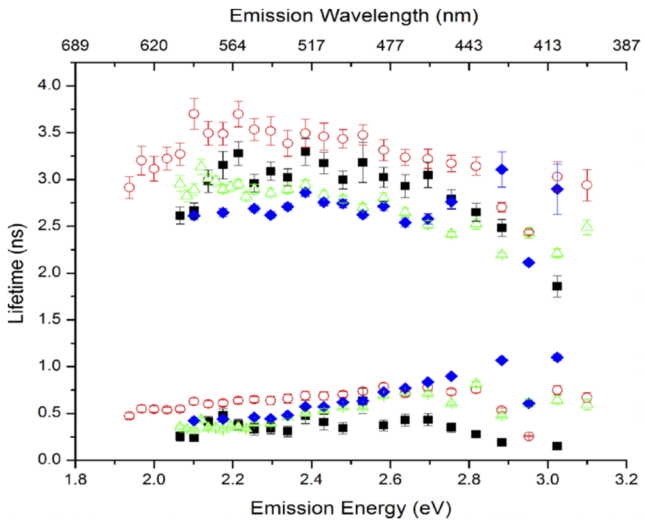

FIG. 3. The radiative lifetime at different detection photon energies and different solvents and orientations of the detection slit. The error bars shown represent the standard deviation in the lifetime fitting parameters.

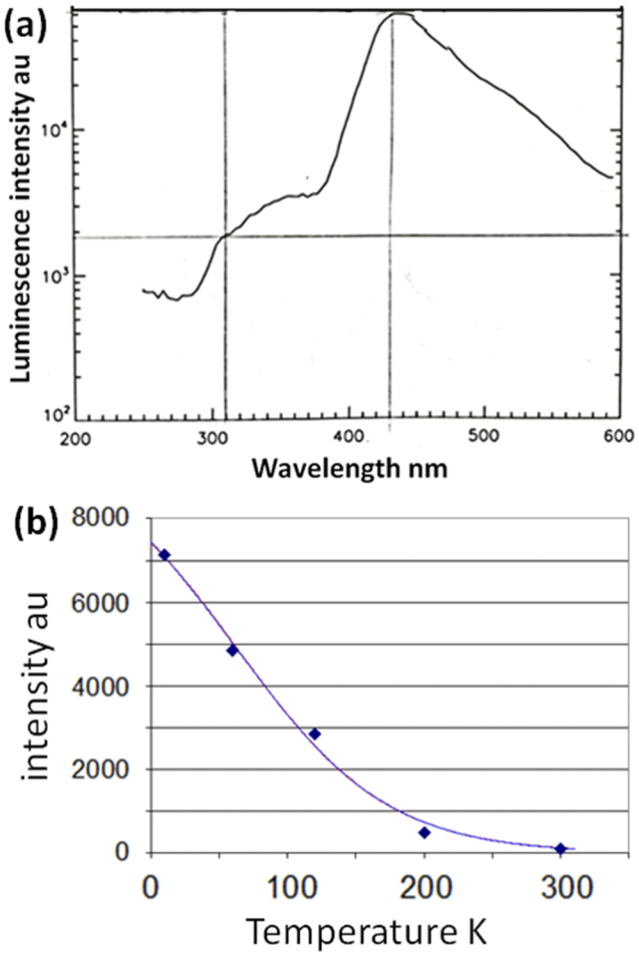

FIG. 4. Photoluminescence from the hydrogenated 1.0-nm nanoparticles ($Si_{29}H_{24}$) taken under continuous wave (CW) synchrotron radiation. (a) The luminescence spectrum over the range of 250–650 nm, with the sample cooled to 10° K, and under excitation with the incident photon energy of 5.4 eV. The spectrum shows multiple wide luminescence bands in the UV at 265, 310, and 350 nm, as well as a visible band in the deep blue. (b) Intensity at the peak of the blue band at 430 nm as a function of temperature in the range of 300°–10° K. The fitting curve is a two internal crossing model fit (excited singlet-excited triplet crossing and excited triplet-ground singlet crossing). The fit uses activation energy of 1300°–1500°K.

maximum down to the lowest temperature of 10° K accessible in our experiment. Figure 4(b) shows that the intensity of the blue luminescence band exhibits an enhancement of two orders of magnitude at 10° K compared to room temperature. The increase of luminescence at a lower temperature is pivotal for cooling applications in view of the fact that for a rare-earth-doped system, the population at the top of the ground state manifold of energy levels dramatically decreases as the temperature drops below 100° K, strongly reducing the efficiency of the cooling process.[46–50] In addition to the triplet crossing effect, the increase in the quantum efficiency with temperature reduction can be impacted by the statistics of the system. Contrary to rare-earth-doped systems, in the nanosilicon material, the quantum efficiency increases with a decrease in the temperature all the way to 10° K, as studied in this experiment. Unlike implanted ions, the lower energy valence band of silicon is expected to be populated even at temperatures close to absolute zero because they are governed by Fermi–Dirac statistics.[46–50]

D. Excitation measurements (nanosilicon transparency)

Figure 5 presents (in green) on the lower left our measurement of the excitation spectrum as a function of the incident photo-energy over the range of 5–13 eV while monitoring the luminescence at 430 nm. Superimposed is a plot of the photo-absorption spectrum calculated using time-dependent density functional theory (TDDFT) in the energy range of 0–25 eV.[55] The luminescence intensity (vertical scale) is arbitrary while the luminescence photon energy (horizontal scale) is the same as that of the absorption scale. Excitation spectra are effectively the product of the absorption and the luminescence quantum efficiencies. Beyond 13 eV (not shown), the excitation spectrum falls slowly and somewhat smoothly. Figure 5 shows that the strongest luminescence is at 6.3 eV when the absorption is only 8% of the maximum absorption (at ~9.0 eV), i.e., the strongest excitation is not when the absorption is the strongest. It is to be noted that in the experiment, the absorption at the incident photon energy and the observed anti-Stokes scattering is only 0.17% of the maximum absorption of the film (at ~9.0 eV).

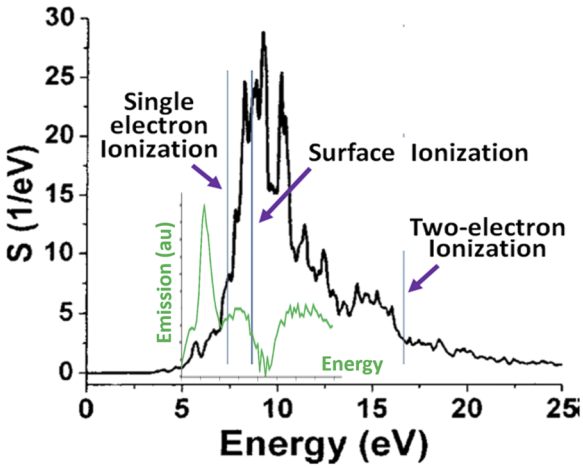

FIG. 5. Photo-absorption spectrum S of hydrogenated 1.0-nm nanoparticles ($Si_{29}H_{24}$) calculated using TDDFT in the photon energy range of 0–22 eV.[48] The population right of the absorption (in black) is adapted from Rao *et al.*, Phys. Rev. B **69**, 205319 (2004). Copyright 2004 American Physical Society. Superimposed on the lower (in green) is our measurement.

This measurement shows that this configuration design provides a convenient compromise between absorption, emission, and transparency. This is important for cooling applications since *it is to be noted that the* transparency at the working frequency in a cooling system is a pivotal condition for successful photo-cooling of solid samples. Transparency to luminescence/scattering photons reduces heating in the bulk of the film. Post loss to heat and availability of the light source with high intensity, significantly minimizing re-absorption of the luminescence, may cause post absorption and heating effects. In other words, this minimizes light re-absorption and trapping, hence allowing high efficiency of extraction of the light and preventing heating effects. In the case of films of 1-nm silicon nanoparticles, the widening of the gap from 1.1 eV to nearly 3.3–3.4 eV due to quantum confinement makes the 1-nm nanoparticles nearly 100% transparent (or blind) in the infrared, visible, and near UV (wavelengths $\lambda > 370$ nm).

IV. THEORETICAL SIMULATIONS

A. Atomistic calculations of the molecular-solid structure

To analyze the thermo–time dynamics in 1-nm particles, we must calculate the relevant molecular structure and energy levels of the particle. Since in the experimental preparation, the 1-nm particles come in different surface re-construction conditions ($Si_{29}H_x$) where x is the number of hydrogen atoms (36-x is twice the number of dimer structures) on the surface shell, we calculated the structure of $Si_{29}H_{24}$ and $Si_{29}H_{34}$, corresponding to six-dimers and one-dimer cases, respectively. We used the General Atomic and Molecular Electronic Structure System (GAMESS) quantum chemistry computation package[56,57] with the time-dependent density functional theory method using the local density approximation (TDLDA). The ground and first excited states were calculated in the 6-311G** basis set[58] using the Becke three-parameter non-local exchange functional[59] with the Lee, Yang, and Parr non-local electron correlation functional (B3LYP).[60] Figure 6(a) shows the energy surfaces of the ground and first excited states along with oscillator strengths for the six-dimer case (fully re-constructed surface) as a function of the inflated dimer bond *R*. It shows the presence of an inter-well potential barrier at ~0.3 nm, separating two regions. Below 0.3 nm is bulk-like and above 0.3 nm is molecular-like. Figure 6(b) shows the corresponding lifetimes obtained from the oscillator strengths. The calculated spectra show that the fast lifetime of luminescence drops rapidly as we approach the barrier where the radiative nature begins, then it becomes flat, which indicates that, in the region of interest of 2.8 eV, the response is nearly independent of wavelength (the wavelength response is flat response) in agreement with the present measurements.

The lifetime plot in Fig. 6(b) shows that it swings from a second scale (which is considered as good as infinitely long) to a nanosecond scale, which is representative of fast emitting materials. The long lasting emission emanates from the tetrahedral part of the structure (core), which is mostly in the interior of the particle.

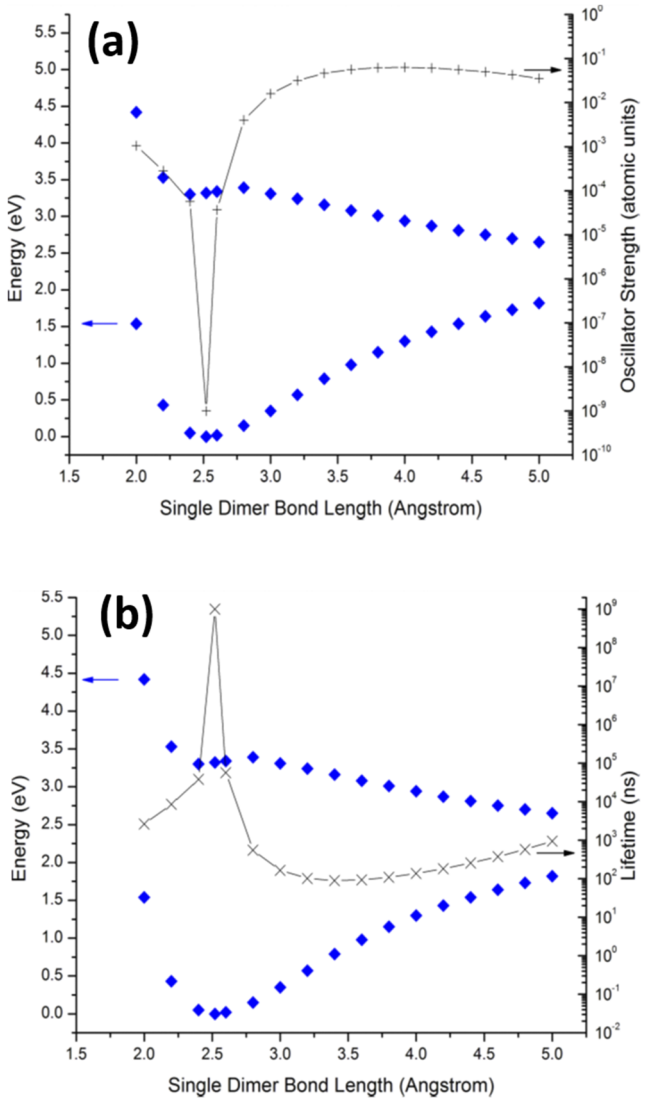

FIG. 6. Atomistic calculation of the molecular structure of the 1-nm nanoparticle with different surface reconstruction conditions (the number of surface dimers) as a function of the inflated dimer bond *R*. (a) Ground and first excited singlet energy surfaces of $Si_{29}H_{24}$ (six dimers) optimized individually using TD-DFT along the reaction coordinate of the dimer bond *R*, with the corresponding oscillator strength. The barrier height is 90 meV. (b) Corresponding lifetimes obtained from the oscillator strengths plotted on the energy level diagram.

The long lifetime in the tetrahedral part is due to the fact that quantum mechanically the emission is forbidden due to the tetrahedral (TD) symmetry that dictates zero transition dipole moment. The fast emission emanates from the molecular dimer-like part (shell) near and beyond the potential barrier, which is located on the surface of the particle.

B. Triplet temperature dependence

We now examine the impact of triplet crossings on the temperature dependence of blue luminescence. A prospective mechanism is based on the singlet-triplet state crossings. The existence of singlet-triplet crossings was established using time-dependent density functional theory (TDDFT) atomistic calculations and simulations.[61–63] We approximate the particle by a restricted three-level (-state) system: ground singlet state, excited singlet state, and excited triplet state. The mechanism is based on the crossing of the lowest triplet state with the lowest singlet state as well as with the ground state (singlet). We set up the rate equations for the interaction of the system, with n_s, n_t, and n_g being the population densities for the excited singlet state, excited triplet state, and ground singlet state, respectively. In the model, optical excitation, at high lying singlet states, populates the lowest singlet. The singlet is coupled to the triplet state through thermal activation and to the ground state via absorption and emission of radiation and non-radiative recombination. The triplet state is coupled to the ground state via electron scattering at the crossing point (re-circulate the population back to the singlet part of the system) and to the singlet state through electron scattering and thermal activation. The population constraint is $n_s + n_t + n_g = n_0$. The population and final luminescence spectrum is a result of these competing coupled processes. Solving the rate equations in the steady state limit gives the following expression for the intensity:

$$\text{Intensity} = IR_0/(1 + R_m\text{Exp}[T/T_m](R_a + R_c)/(R_{emi}(R_t\text{Exp} \times [-T_r/T] + R_c)) + (R_a + R_n\text{Exp}[T/T_n])/R_{emi}),$$

where the parameters are defined as follows: R_a is the rate of absorption from the ground state to the excited singlet state, R_{emi} is the radiative rate from the excited singlet state to the ground state, resulting in the emission of a photon, and $R_n = R_{n0}\,\text{Exp}[T/T_n]$ is the non-radiative rate from the excited singlet state to the ground state, resulting in heat. The rest of the rates involve the triplet state. R_m is the rate of mixing of the excited singlet with the excited triplet due to collisions, $R_t = R_{t0}\,\text{Exp}[-T_r/T]$ is the thermal activation rate from the triplet to the excited singlet, and R_c is the rate of conversion down from the triplet to the ground state at the crossing point of the extended bond. We used the activation energy in the range of 1300°–1500°K. Figure 5(b) shows the experimental results and the fit to the data using this model.

C. Thermal emission above barrier

A delay in the onset of luminescence with temperature was observed in Fig. 2(b). We analyze this temperature dependence of the emission using inter-well barrier thermal activation of the one-dimer case. For this case, a harmonic extension of the outer well was used to extend the potential beyond the range of dimer separations considered. We then numerically solved for the double well eigenenergies,[64] as shown in Fig. 7(a). We assume that, upon UV excitation, the nanoparticle begins in the inner well and quickly forms a quasi-equilibrium with the solvent. The thermal statistical distribution of energies measured from the inner well equilibrium follows a Boltzmann distribution of the form

$$P(\varepsilon, T) = \frac{g(\varepsilon)e^{-\varepsilon/kT}}{Z(T)}, \quad (1)$$

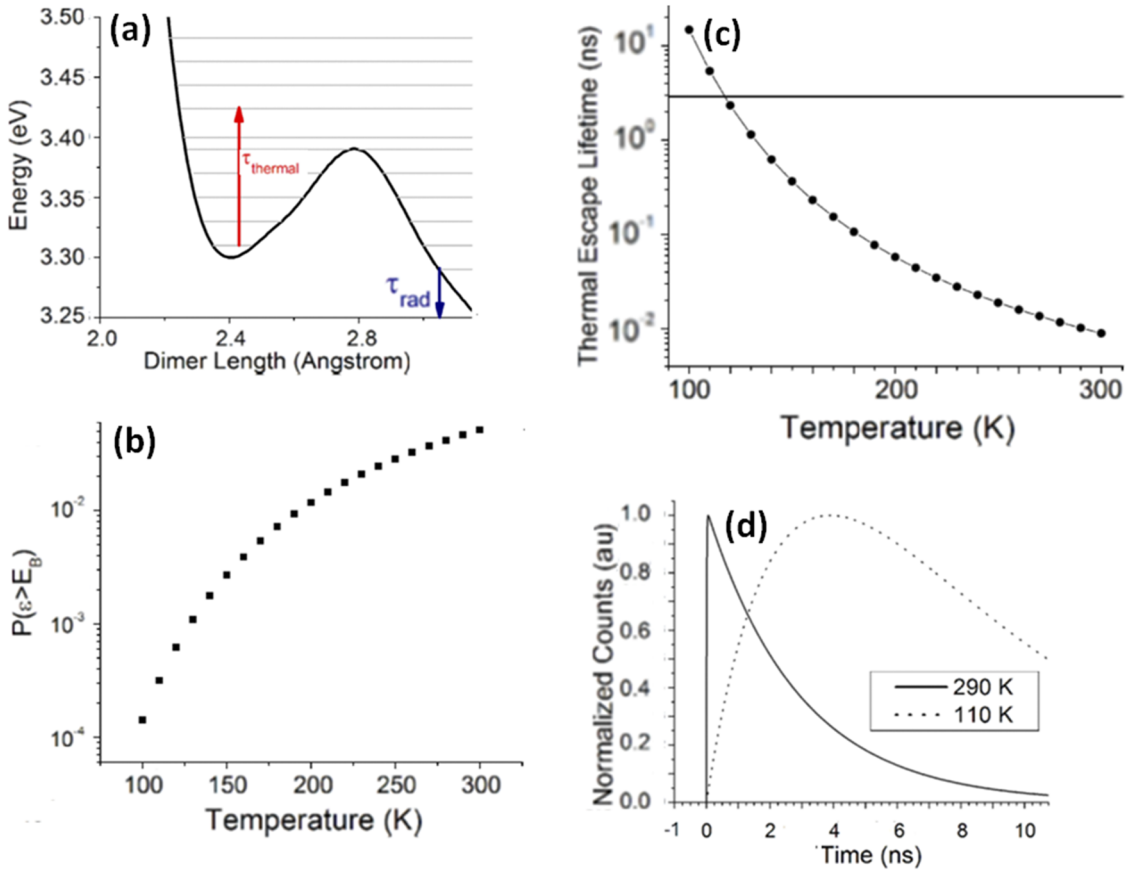

FIG. 7. (a) Numerically solved double well vibration eigenenergies *in the six*-dimer structure. We assume that upon UV excitation, the nanoparticle begins in the inner well, with τ_{th} being the lifetime for thermal excitation over the inter-well barrier and τ_{rad} being the lifetime for emission of a photon from the outer well. (b) Calculated Boltzmann probability for finding the system with an energy above the inter-well barrier as a function of temperature for the six-dimer particle. (c) Calculated temperature dependence of these thermal escape lifetimes. The curves represent the escape probability at the $1 - e^{-1}$–0.632 level (dot). The measured average radiative lifetime of 2.9 ± 0.2 ns is shown for reference (solid line). (d) Predicted time traces at the highest (290° K) and lowest experimental temperatures (110° K) for a barrier of 90 meV.

$$Z(T) = \sum_{\varepsilon=0}^{\infty} g(\varepsilon) e^{-\frac{\varepsilon}{kT}}, \tag{2}$$

where $g(\varepsilon)$ is the degeneracy at energy E. We treat the problem as a one-dimensional system with the dimer bond length as the generalized coordinate so that each nuclear vibrational level will be singly degenerate, making $g\ (\varepsilon) = 1$. The probability of attaining an energy greater than the barrier height E_B is then

$$P(\varepsilon > E_B, T) = \frac{1}{Z(T)} \sum_{\varepsilon=E_B}^{\infty} e^{-\varepsilon/kT} \tag{3}$$

$$\approx \frac{1}{Z(T)} \sum_{\varepsilon=E_B}^{E_{\max}} e^{-\varepsilon/kT}, \tag{4}$$

where $E_{\max}$ is a cutoff energy chosen so the probability of occupation $P\ (E_{\max};T)$ from Eqs. (1) and (2) is less than 10^{-5} of $P\ (E_B;T)$. These total system eigenenergies were then inserted into Eqs. (3) and (4). The resultant probability of finding the system with an energy above the inter-well barrier is plotted as a function of temperature in Fig. 7(b).

A simplified model of this scenario proceeds in two steps: first, the system forms an initial quasi-equilibrium distribution in the inner well, creating a Boltzmann distribution of energies. Second, any states with $E > E_B$ are assumed to escape the inner well with 100% probability and immediately be transferred to the outer well. The probability to subsequently remain in these states is, therefore, set to zero (mimicking the emission of a photon). Each pass through these two steps is referred to as one "redistribution." In essence, each redistribution renormalizes the total probability to remain in the low-lying states (near the bottom of the inner well for example). For the roughly 20 meV spacing of the energy levels near the inner well minimum, this time is $2\pi/\omega = h/\delta E \sim 0.1$ ps. In this simplified scheme, the number of redistributions n required to leave the well with a target probability may be calculated according to the following expression:

$$(1 - P_{target}) = (P_{remain})^n \Rightarrow \tag{5}$$

$$n = \frac{\ln(1 - P_{target})}{\ln P_{remain}}, \tag{6}$$

$$P_{remain} = \frac{1}{Z(T)} \sum_{\varepsilon < E_B} e^{-\varepsilon/kT}. \tag{7}$$

Multiplying the required number of redistributions by the estimated timescale for a single redistribution generates an order of magnitude estimate of the time required for the excited nanoparticle to escape the inner well thermally. Using a target probability to leave the well of $1 - e^{-1}$ generates the estimated thermal escape lifetime. Figure 7(c) summarizes the temperature dependence of these thermal escape lifetimes. The estimated thermal escape lifetimes become comparable to the measured radiative lifetime of 2.9 ns at temperatures below ~130° K.

As shown in Fig. 7(a), we designate τ_{th} as the lifetime for thermal excitation over the inter-well barrier and designate τ_{rad} as the lifetime for the emission of a photon from the outer well. Following the experimental results, we choose τ_{rad} = 0.9 ns. Moreover, the radiative lifetimes are assumed to be temperature independent, as the experimental data above showed no appreciable change with temperature, while we take τ_{th} to be temperature dependent.

We represent the two subsequent first-order decays using a rate equation model. An initial excitation into the bottom of the inner well reaches an energy above the barrier with a characteristic time τ_{th}. After some thermal relaxation, the nanoparticle subsequently emits a photon from the outer well with radiative lifetime τ_{rad}. Mathematically, the relations appear as

$$Inner\ Well \xrightarrow{k_{th}} Outer\ Well \xrightarrow{k_{rad}} Ground\ State,$$

$$\frac{dN_I}{dt} = -k_{th} N_I, \tag{8}$$

$$\frac{dN_O}{dt} = k_{th} N_O, \tag{9}$$

where N_I and N_O are the number of nanoparticles in the inner and outer wells and the rate constants k_{th} and k_{rad} are $1/\tau_{th}$ and $1/\tau_{rad}$, respectively. We have assumed that there is no feedback from the outer well back to the inner well. These coupled equations have the solution

$$N_I(t) = N_{IO} e^{-t/T_{th}}, \tag{10}$$

$$N_O(t) = N_{O0} e^{-t/T_{rad}} + \frac{N_{I0}}{1 - \frac{T_{th}}{T_{rad}}} \left(e^{-\frac{t}{T_{rad}}} - e^{-\frac{t}{T_{th}}} \right), \tag{11}$$

where N_{I0} and N_{O0} are the initial numbers of nanoparticles in the inner well and outer well at the moment of excitation, respectively. Since the experimental excitation energy promotes nanoparticles to low-lying inner well states, the initial number of nanoparticles in the outer well is set to zero. This is in accordance with the Franck–Condon principle in which absorption or emission of a photon in a molecule (undergoing an electronic transition) of the nuclear configuration experiences no significant change. In other words, since absorption and emission are very fast processes, the inter-nuclear distance does not change, and thus the transitions are represented as vertical lines. The projected theoretical emission time trace is then given by the second term in Eqs. (10) and (11).

Figure 7(d) shows the predicted time traces at the highest and lowest experimental temperatures using this expression with the estimated τ_{th} from Figs. 7(b) and 7(c). At room temperature, the thermal escape lifetime is much faster than the radiative recombination time. The outer well state is populated quickly, climbing to the peak emission strength rapidly. In contrast, at 110° K, the thermal excitation lifetime (4 ns) is longer than the radiative lifetime. The rise to the peak emission strength is much slower, leading to a maximum in the time.

Thermal escape times were calculated with Eqs. (5)–(7) using several different energy barrier heights. Since the outer well is much wider and deeper than the inner well, the energy level spacing was assumed to be relatively unaffected by altering the barrier height. The resulting thermal escape lifetimes as a function of temperature and different barrier heights are shown in Fig. 8(a). Using these estimates for the thermal escape lifetimes, we calculate an array for the onset as a function of temperature and different barrier heights. The results show that the best fit is for a barrier

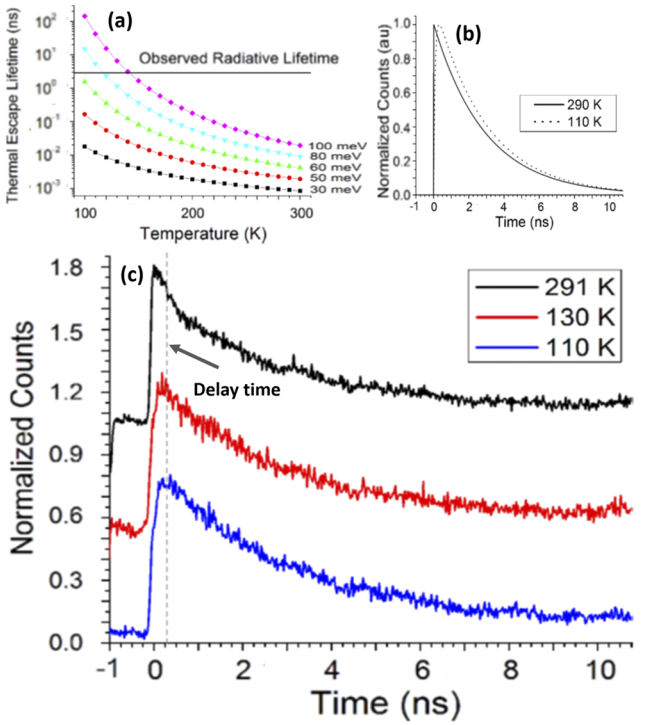

FIG. 8. (a) Thermal escape times calculated using several different energy barrier heights. (b) Predicted time traces at the highest (290° K) and lowest experimental temperatures (110° K) for a barrier of 50 meV. (c) Time traces of the experimental data (top-to-bottom) at temperatures of 290°, 180°, and 130° K, respectively, along with the calculated shift of the onset of luminescence at a low temperature showing good agreement. The estimated thermal escape lifetimes become comparable to the measured radiative lifetime of 2.9 ns at temperatures below ~130° K.

height of 50 meV. Figure 8(b) shows the calculated time dynamics at 290° and 110° for a 50 meV barrier height. We see a shift of 0.29 ± 0.08 ns at 110° K. This agrees well with the experimental value of 0.28. Figure 8(c) shows the experimental data [reproduced from Fig. 3(b)] along with this result, showing excellent agreement. While the calculated barrier height of 90 meV is larger than the data warrant, the localized wave functions in the outer well are qualitatively consistent with short lifetimes. Simple dimer stretching, therefore, appears to give a good qualitative picture of the nature of silicon nanoparticle radiative recombination but does not accurately predict the recombination dynamics. The measured lifetimes and temperature-dependent fluorescence time traces both require molecular rearrangements with much faster lifetimes and smaller relaxation energy barriers than this simplistic model predicts. As the TDLDA calculations performed in this work considered only simple dimer stretching under $C2v$ symmetry, there well exist more complicated relaxation pathways between the inner and outer well states, which reduce or even circumvent the inter-well barrier.

In fact, recent advances in excited state simulation and relaxation strategies showed that the barrier traps excitation into the indirect channel, hindering emission. Enlarging the number of dimers reduces the potential barrier monotonically to a finite limit not sufficient for strong emission to proceed. However, being trapped in the excited state, the particle experiences strong strain and structural instability, which triggers non-radiative, structural relaxation to lower energy manifolds, allowing the trapped energy to be strongly released radiatively, i.e., creating a direct path for emission without crossing the barrier and effectively mimicking the lowering of the barrier.[33]

The time delay observed is in agreement with the calculated delays using the model. The emission is fast but the population transfer is sensitive to temperature. It shows that the buildup of the population of the emitting state is faster at a higher temperature. This is indeed consistent with the presence of a potential barrier between the absorption and emission channels. It is to be noted that the emission spectra are found to be largely independent of excitation energy in the range from 4.6 eV up to 7.5 eV. However, in this range, above barrier excitation takes place followed by relaxation to the top of the barrier region.

V. DISCUSSION

It is interesting to mention that the 1-nm silicon nanoparticles were previously reconstituted into microcrystallites on device-quality Si.[40] The film was excited at room temperature by a near-infrared laser in the range of 750–830 nm with the radiation focused to ~1 μm. The procedure employed a two-photon excitation process in normal incidence using a mode-locked femtosecond Ti:sapphire pulses of 150 fs pulse duration and peak intensity of 2×10^{10} -4×10^{12} W/cm^2. The response shows narrow radiation at half the incident wavelength with the peaks (second harmonic). The power dependence of the emission recorded showed a quadratic response. Ionic vibration of or/and excitonic trapping on the radiative Si–Si dimer phase, found only in ultrasmall nanoparticles, were suggested as a basic mechanism for inducing anharmonicity that breaks the centrosymmetry. Although the results were discussed in terms of second-harmonic generation, it was noted that bulk silicon is known to have negligible nonlinearity, being zero at the second order level (not allowed) and very small at the third order level. It was also noted that no measurable harmonic generation from control Si substrates with no nanoparticles deposited. The spectra also show anti-Stokes scattering peaks at blue-shifted by 10 nm from the second harmonic peak.

The response from different parts of the film reveals some relationship between the second harmonic and the luminescence. Spectra, in general, have a harmonic peak, a blue band, and a weaker green/yellow band. The harmonic peak anti-correlates with the blue band but correlates with the green/yellow band. Those anti-Stokes results are believed to be a special case of the general case of coherent anti-Stokes Raman scattering (CARS).[7] In the CARS process, an incident pump laser beam (at frequency ω_{pump}) and an incident Stokes laser beam (at frequency ω_{Stokes}) interact, producing an anti-Stokes signal at frequency CARS = $2\omega_{pump} - \omega_{Stokes}$. In the present process, there is only one incident beam. The Stokes beam is generated internally. In fact, it has been established in the literature that stimulated anti-Stokes scattering may be generated with only one incident beam (frequency ω_L), while the Stokes field (frequency ω_s) is internally produced. It is observed on the cone-surface with the cone-axis parallel to the wave vector, $\boldsymbol{k}_L$, in contrast to the CARS.

These studies show that luminescence channels may be inhibited dynamically in favor of anti-Stokes scattering (anti-correlates). The results show the disappearance of the luminescence, being replaced by harmonic generation and anti-Stokes scattering. The luminescence is inhibited dynamically in favor of the stimulated nonlinear channels. Coherent anti-Stokes Raman scattering (ASRS) requires phase matching conditions, which require a fundamental structure of the nanoparticles as well as the electromagnetic part of the interaction, including phase matching, in addition to the feedback by the silicon substrate. The mechanism for the second harmonic generation was attributed to the formation of the surface of the intrinsic Si–Si dimer-like bond sites shown in Fig. 6, which breaks the centrosymmetric of bulk silicon, leading to the required non-zero second order susceptibility. This is evidenced by the fact that the inhibition occurs under certain phase matching. The anti-Stokes scattering must be faster than the thermal activation above the barrier and the structural relaxation to be able to inhibit the luminescence to result in cooling.

The increase of luminescence shown in Fig. 4(b) at low temperature may result in an increase in the anti-Stokes scattering when the phase matching conditions for the stimulated anti-Stokes process are satisfied. The anti-Stokes scattering is expected to be enhanced at a lower temperature as we observed a nearly 2-order of magnitude increase in the quantum efficiency of the Stokes luminescence when cooling down to 10° K.

VI. CONCLUSION

We conducted studies of the luminescence strength and the thermo–time-dynamics, over the range of 300°–10°K, of the luminescence of tetrahedral-molecular core–shell 1-nm silicon nanoparticles prepared *ex situ*. The studies used nanoparticles in solution, thin films, and re-crystallized thin solids. We examined the photothermodynamics and time dynamics. We examined the temperature dependence of the quantum efficiency and time dynamics (lifetime and time onset) of the Stokes luminescence band. With the temperature, the measurements give a flat lifetime but with the time delay

in the onset of the photoluminescence in agreement with a model calculation of the above barrier emission. Our results of atomistic TDLDA calculation show that the Stokes heating process takes place in the molecular-like shell where the lifetime is in the nanosecond regime, whereas the anti-Stokes cooling takes place in the tetrahedral core where the lifetime is in the ms regime. Unlike doped glasses, we observed a 2-order of magnitude increase in the quantum efficiency due to Fermi–Dirac statistics and delay in the onset of the Stokes luminescence when cooling down to 10° K, pointing to above-barrier thermal emission. The low-temperature increase in the quantum efficiency of luminescence, accompanied by other characteristics, such as a high quantum efficiency of stimulated anti-Stokes scattering, which anti-correlates with the luminescence, as well as the visible transparency/blindness in nanosilicon are important requirements for solid state photo-cooling. As a result, this may afford an all-silicon photo-cryo-refrigeration, with potential full integration into the CMOS silicon industry.

ACKNOWLEDGMENTS

This paper is in memory of our collaborator on this study, the late Dr. Adam D. Smith of the University of Illinois at Urbana-Champaign, who passed away before the work could have been completed. He conducted extensive research on the time dynamics and temperature dependence of the optical properties of ultrasmall silicon nanostructures.

AUTHOR DECLARATIONS

Conflict of Interest

The authors have no conflicts to disclose.

DATA AVAILABILITY

The data that support the findings of this study are available from the corresponding author upon reasonable request.

REFERENCES

[1] A. Wehrl, Rev. Mod. Phys. **50**(2), 221 (1978).
[2] S. W. Hawking, Phys. Rev. D **32**(10), 2489 (1985).
[3] P. Attard, *Non-Equilibrium Thermodynamics and Statistical Mechanics: Foundations and Applications* (Oxford University Press, Oxford, UK, 2012), p. 1.
[4] G. E. Romero and D. Pérez, Int. J. Mod. Phys. D **20**(14), 2831 (2011).
[5] P. Pringsheim, Z. Phys. **57**, 739 (1929).
[6] T. W. Hänsch and A. L. Schawlow, Opt. Commun. **13**, 68 (1975).
[7] H. Abramczyk, "Anti-Stokes photoluminescence (ASPL)," in *Introduction to Laser Spectroscopy* (Elsevier Science, 2005), p. 1.
[8] L. Landau, "On the thermodynamics of photoluminescence," J. Phys. **10**, 503–506 (1946).
[9] S. V. Boriskina, J. K. Tong, W.-C. Hsu, B. Liao, Y. Huang, V. Chiloyan, and G. Chen, J. Nanophotonics **5**(1), 134 (2016).
[10] R. I. Epstein, M. I. Buchwald, B. C. Edwards, T. R. Gosnell, and C. E. Mungan, Nature **377**, 500 (1995).
[11] C. E. Mungan, M. I. Buchwald, B. C. Edwards, R. I. Epstein, and T. R. Gosnell, Phys. Rev. Lett. **78**, 1030 (1997).
[12] J. L. Clark and G. Rumbles, Phys. Rev. Lett. **76**, 2037 (1996).
[13] C. W. Hoyt, M. Sheik-Bahae, R. I. Epstein, B. C. Edwards, and J. E. Anderson, Phys. Rev. Lett. **85**, 3600 (2000).
[14] M. Sheik-Bahae and R. I. Epstein, Phys. Rev. Lett. **92**, 247403 (2004).
[15] B. Imangholi, M. P. Hasselbeck, R. I. Epstein, and S. Kurtz, Proc. SPIE **6115**, 611518 (2006).
[16] M. Sheik-Bahae and R. I. Epstein, Nat. Photonics **1**, 693 (2007).
[17] E. Finkeißen, M. Potemski, P. Wyder, L. Viña, and G. Wiemann, Appl. Phys. Lett. **75**, 1258 (1999).
[18] G. C. Dousmanis, C. W. Mueller, H. Nelson, and K. G. Petzinger, Phys. Rev. **133**, A316 (1964).
[19] E. H. Kennard, Phys. Rev. **29**, 466 (1927).
[20] J. Yao, D. R. Larson, H. D. Vishwasrao, W. R. Zipfel, and W. W. Webb, Proc. Natl. Acad. Sci. U. S. A. **102**, 14284 (2005).
[21] A. L. Rogach, T. Franzl, T. A. Klar, J. Feldmann, N. Gaponik, V. Lesnyak, A. Shavel, A. Eychmüller, Y. P. Rakovich, and J. F. Donegan, J. Phys. Chem. C **111**, 14628 (2007).
[22] K. I. Rusakov, A. A. Gladyshchuk, Y. P. Rakovich, J. F. Donegan, S. A. Filonovich, M. J. M. Gomes, D. V. Talapin, A. L. Rogach, and A. Eychmüller, Opt. Spectrosc. **94**, 859 (2003).
[23] Y. P. Rakovich, J. F. Donegan, S. A. Filonovich, M. J. M. Gomes, D. V. Talapin, A. L. Rogach, and A. Eychmüller, Physica E **17**, 99 (2003).
[24] S. A. Filonovich, M. J. M. Gomes, Y. P. Rakovich, J. F. Donegan, D. V. Talapin, N. P. Gaponik, A. L. Rogach, and A. Eychmüller, "Up-conversion luminescence in colloidal CdTe nanocrystals," Mater. Res. Soc. Symp. Proc. **737**, 157–162 (2003).
[25] Y. P. Rakovich, S. A. Filonovich, M. J. M. Gomes, J. F. Donegan, D. V. Talapin, A. L. Rogach, and A. Eychmüller, Phys. Status Solidi B **229**, 449 (2002).
[26] A. G. Joly, W. Chen, D. E. McCready, J.-O. Malm, and J.-O. Bovin, Phys. Rev. B **71**, 165304 (2005).
[27] X. Wang, W. W. Yu, J. Zhang, J. Aldana, X. Peng, and M. Xiao, Phys. Rev. B **68**, 125318 (2003).
[28] E. Poles, D. C. Selmarten, O. I. Mićić, and A. J. Nozik, Appl. Phys. Lett. **75**, 971 (1999).
[29] W. Chen, A. G. Joly, and D. E. McCready, J. Chem. Phys. **122**, 224708 (2005).
[30] M. J. Fernée, P. Jensen, and H. Rubinsztein-Dunlop, Appl. Phys. Lett. **91**, 043112 (2007).
[31] J. M. Harbold and F. W. Wise, Phys. Rev. B **76**, 125304 (2007).
[32] J. Gieseler, R. Quidant, C. Dellago, and L. Novotny, Nat. Nanotechnol. **9**(5), 358 (2014).
[33] K. Mantey, H. Morgan, J. Boparai, Z. Yamani, E. Bahceci, and M. H. Nayfeh, AIP Adv. **11**, 095319 (2021).
[34] A. N. Pearson, Y. Guryanova, P. Erker, E. A. Laird, G. A. D. Briggs, M. Huber, and N. Ares, Phys. Rev. X **11**, 021029 (2021).
[35] M. Lannoo, C. Delerue, and G. Allan, J. Lumin. **70**, 170 (1996).
[36] M. I. Baratron, *Functionalization, and Surface Treatment of Nanoparticles* (American Scientific Publishers, 2002).
[37] M. H. Nayfeh and L. Mitas, "Silicon nanoparticles. New photonic and electronic material at the transition between solid and molecule," in *Nanosilicon*, edited by V. Kumar (Elsevier, 2007).
[38] M. H. Nayfeh, *Fundamentals and Applications of Nano Silicon in Plasmonics and Fullerenes: Current and Future Trends* (Elsevier Publishing, 2018), p. 1.
[39] M. H. Nayfeh, M. Alamri, M. M. El Gomati, and M. S. Zubairy, "Optics in nanotechnology," in *Optics in Our Time* (Springer, 2016), p. 223.
[40] M. H. Nayfeh, O. Akcakir, G. Belomoin, N. Barry, J. Therrien, and E. Gratton, Appl. Phys. Lett. **77**, 4086 (2000).
[41] M. H. Nayfeh, N. Barry, J. Therrien, O. Akcakir, E. Gratton, and G. Belomoin, Appl. Phys. Lett. **78**, 1131 (2001).
[42] M. H. Nayfeh, S. Rao, N. Barry, J. Therrien, G. Belomoin, A. Smith, and S. Chaieb, Appl. Phys. Lett. **80**, 121 (2002).
[43] S. Magill, J. Xie, M. Nayfeh, H. Yu, M. Fizari, J. Malloy, and Y. Maximenko, J. Instrum. **10**, P05008 (2015).
[44] M. H. Nayfeh, S. Rao, O. M. Nayfeh, A. Smith, and J. Therrien, IEEE Trans. Nanotechnol. **4**, 660 (2005).
[45] K. Mantey, L. Quagliano, A. Rezk, S. Palleschi, L. Abuhassan, A. Nayfeh, E. Bahceci, and M. H. Nayfeh, AIP Adv. **11**, 105206 (2021).
[46] F. Reif, *Fundamentals of Statistical and Thermal Physics* (McGraw-Hill, 1965), ISBN: 978-0-07-051800-1.

[47]J. S. Blakemore, *Semiconductor Statistics* (Dover, 2002), ISBN: 978-0-486 -49502-6.
[48]C. Kittel, *Introduction to Solid State Physics*, 4th ed. (John Wiley & Sons, New York, 1971).
[49]E. Fermi, "Sulla quantizzazione del gas perfetto monoatomico," Rend. Lincei **3**, 145–149 (1926) (in Italian), translated as A. Zannoni "On the quantization of the monoatomic ideal gas," arXiv:cond-mat/9912229 (1999).
[50]P. A. M. Dirac, Proc. R. Soc. A **112**(762), 661–677 (1926).
[51]O. Ackakir, J. Therrien, G. Belomoin, N. Barry, J. Muller, E. Gratton, and M. Nayfeh, Appl. Phys. Lett. **76**, 1857–1859 (2000).
[52]G. Belomoin, J. Therrien, A. Smith, S. Rao, R. Twesten, S. Chaieb, M. H. Nayfeh, L. Wagner, and L. Mitas, Appl. Phys. Lett. **80**, 841 (2002).
[53]D. Nielsen, L. Abuhassan, M. Alchihabi, A. Al-Muhanna, J. Host, and M. H. Nayfeh, J. Appl. Phys. **101**(11), 114302 (2007).
[54]S. Rao, J. Sutin, R. Clegg, E. Gratton, M. H. Nayfeh, S. Habbal, A. Tsolakidis, and R. M. Martin, Phys. Rev. B **69**, 205319 (2004).
[55]A. Smith, Z. Yamani, J. Turner, S. Habbal, S. Granick, and M. H. Nayfeh, "Observation of strong direct-like oscillator strength in the photoluminescence of 1 nm silicon nanoparticles," Phys. Rev. B **72**, 205307 (2005).
[56]M. W. Schmidt, K. K. Baldridge, J. A. Boatz, S. T. Elbert, M. S. Gordon, J. H. Jensen, S. Koseki, N. Matsunaga, K. A. Nguyen, S. Su, T. L. Windus, M. Dupuis, and J. A. Montgomery, J. Comput. Chem. **14**, 1347 (1993).
[57]M. S. Gordon and M. W. Schmidt, "Advances in electronic structure theory: GAMESS a decade later," in *Theory and Applications of Computational Chemistry* (Elsevier, Amsterdam, 2005).
[58]R. Krishnan, J. S. Binkley, R. Seeger, and J. A. Pople, J. Chem. Phys. **72**, 650 (1980).
[59]A. D. Becke, "Density-functional thermochemistry. III. The role of exact exchange," J. Chem. Phys. **98**, 5648 (1993).
[60]C. Lee, W. Yang, and R. G. Parr, Phys. Rev. B **37**, 785 (1988).
[61]M. Palummo, F. Iori, R. Del Sole, and S. Ossicini, Phys. Rev. B **81**, 121303 (2010).
[62]O. Lehtonen and D. Sundholm, Phys. Rev. B **72**, 085424 (2005).
[63]J. Malloy, K. Mantey, Y. Maximenko, E. Bahceci, H. Morgan, Z. Yamani, J. Boparai, K. Puthalath, and M. H. Nayfeh, J. Appl. Phys. **124**, 044501 (2018).
[64]M. H. Nayfeh, N. Rigakis, and Z. Yamani, Phys. Rev. B **56**, 2079 (1997).